Title

Mechanical and creep properties of granitic minerals of albite, biotite, and quartz at elevated temperature

Authors

Espinoza, Wilson F

Pereira, Jean-Michel

Kneafsey, Timothy

et al.

Publication Date

2023-06-01

DOI

10.1016/j.gete.2023.100465

Peer reviewed

Prepared for *Geomechanics for Energy and the Environment*
Figures: 11
Tables: 0
Words: 4570

Title

Mechanical and creep properties of granitic minerals of albite, biotite, and quartz at elevated temperature

Authors

Wilson F. Espinoza [1,2], Jean-Michel Pereira [3], Timothy Kneafsey [4], Sheng Dai [1],

1 School of Civil and Environmental Engineering, Georgia Institute of Technology
2 College of Science and Engineering, Texas State University
3 Navier, Ecole des Ponts, Univ Gustave Eiffel, CNRS, Marne-la-Vallée, France
4 Energy Geosciences Division, Lawrence Berkeley National Laboratory

Abstract

Fundamental mechanical and creep behavior of minerals at elevated temperatures is relevant to many subsurface exploration and resource recovery processes, yet remains largely elusive. This study uses instrumented indentation to measure microscale deformation and nanoscale creep of biotite, albite, and quartz, which are the major mineral phases of granitic rocks, at temperatures up to 400 °C. The results show that the elastic modulus of biotite is not only the lowest at room temperature but also decays the most at elevated temperature (i.e., by 25% reduction at 400 °C) compared to that of albite and quartz. The creep deformation within 20 s doubles when the temperature increases from 20 °C to 400 °C for albite, quartz, and biotite, and biotite showed at least three times the overall creep deformation compared to quartz and albite under the same temperature. The indentation creep deformation can be well characterized using a logarithmic time model, showing both transient and constant-rate creep deformation. The secondary creep rate for biotite is about three times that of albite and quartz at the same temperature, and as the temperature increases from 20 °C to 400 °C, the rate of secondary creep becomes approximately 10 times faster for the three tested minerals. Both transient creep deformation and the rate of secondary creep can be empirically correlated to the elastic moduli, which allows quick estimates of the temperature-dependent creep behavior of granitic minerals using their elastic properties, especially when those creep constants are not readily available at elevated temperatures. These results enhance the understanding of temperature-dependent creep deformation at small scales and provide insight into mineral-level damage in granitic rocks due to temperature and long-term deformation.

Keywords:

Granite, biotite, temperature, creep, indentation

1 Introduction

Understanding material behavior at constant stress is of interest in multiple disciplines and materials such as metals, polymers, ceramics, composites, concrete, and rocks [*Brinson and Gates*, 1995; *Cannon and Langdon*, 1983; *Evans and Wilshire*, 1985; *Griggs*, 1939; *Kassner*, 2015; *Sorelli et al.*, 2008]. Most studies regarding the mechanical response of materials measured along multiple timescales aim to predict the serviceability of materials used in structural elements of machinery or infrastructures subjected to long-term mechanical or thermal loading. Engineering applications such as underground structures, mining sites, and rock slopes are subjected to stress levels and environmental effects that compromise their stability through creep deformation. The success of nuclear waste disposal sites, carbon sequestration facilities, and enhanced geothermal systems, which are important contributors to the reduction of current and future carbon footprint, relies on the ability of host rock formations to remain serviceable and structurally competent along the geological times. Hence, studying the time-dependent long-term deformation of rocks contributes to accelerating the deployment of these technologies that reduce the environmental risks of energy production and safely store hazardous materials in the subsurface.

Long-term constant stress tests have shown unstable crack propagation caused by slip mechanisms on clay particles rather than by the mechanical instability of quartzitic minerals within the structure of some sedimentary formations [*Fabre and Pellet*, 2006]. Salt rocks have the most notorious creep deformation, attributed to dislocation at the grain scale in forms of glide, climb, and cross-slip [*Urai et al.*, 1986]. Quite a few constitutive models to describe creep deformation in salt rock have been developed in the past decades [*Fei et al.*, 2021; *Firme et al.*, 2018; *Firme et al.*, 2016; *Wu et al.*, 2019; *Zhou et al.*, 2011]. Creep deformation in crystalline rocks is influenced by confining stress [*Kranz*, 1980; *Kranz and Scholz*, 1977], water content [*Fujii et al.*, 1999; *Lockner*, 1993; *Masuda et al.*, 1988], and stress and strain rate [*Fujii et al.*, 1999; *Lin et al.*, 2009; *Masuda et al.*, 1987]. The mechanisms to estimate damage in crystalline rocks consider stress corrosion and fracturing events measured and predicted as a function of strain measurements and acoustic emissions [*Fujii et al.*, 1999; *Lin et al.*, 2009; *Yanagidani et al.*, 1985]. These experimental studies on crystalline rocks explore testing conditions to measure damage within mesoscale configurations, tracking fracture generation and propagation within granite structures. Experimental considerations on the possible effects of grain-scale mineral deformation, mineral interaction, and their contribution to creep deformation at elevated temperatures remain largely elusive.

Some attempts to discretize rock behavior have used numerical approaches that predict the time to failure of rock specimens under triaxial conditions through grain boundary models [*Wang and Cai*, 2020]. Simplifications of grain distributions such as the Voronoi polygonal structure have been useful to simulate the intergranular interaction of crystalline rocks [*Ghazvinian et al.*, 2014; *Liu et al.*, 2018; *Wu et al.*, 2018]. Other studies model creep deformation based on the viscoelasticity or viscoplasticity of materials including rocks and metal composites [*Cristescu*, 2012; *Cristescu and Hunsche*, 1998; *Perzyna*, 1966]. However, simplifications on the heterogeneity of inter-mineral structures may improperly estimate important characteristics of mechanical behavior, especially during long-term creep deformation. Recently, the indentation technique has been deployed to investigate the creep behavior in heterogeneous coal materials [*Sun et al.*, 2020], hard minerals such as quartz considering mineral asperities [*Goldsby et al.*, 2004], and post-seismic transitory creep of quartz-rich rocks whose deformation mechanism is governed by dissolution processes [*Gratier et al.*, 2009]. Nanoscale indentation to understand the creep and mechanical characteristics of natural minerals for granitic rocks has not been fully explored.

This study uses instrumented indentation to measure microscale deformation and nanoscale creep of biotite, albite, and quartz, which are the major mineral phases of granitic rocks. The mechanical performance of these minerals is tested at temperatures up to 400 ^{0}C and their time-dependent deformation is described by models that characterize both transient and steady-state creep. The results are useful to understand the temperature-dependent creep deformation at small scales and provide insight into mineral-level damage in granitic rocks due to temperature and long-term deformation.

2 Experimental design

2.1 Testing procedure

Samples tested in this study include albite, quartz, and biotite, which are typical mineral phases of granite composites in nature. All samples were cut using a 0.3 mm precision wafer blade installed on an Isomet-1000 cutting station. To ensure sample flatness during indentation testing, the minerals were subjected to two subsequent cuts that produced testing disks with 7mm of height. After cutting, all surfaces were polished using a sequence of sandpaper sheets with grits P800, P1200, and P2400, corresponding to averaged grit diameters of 25.8μm, 15.3μm, and 6.5μm, respectively.

After polishing, tested samples were fixed into a three-point chuck-grip holder installed into a furnace mounted on the base of the indenter frame. The sample holder prevented induced errors produced by improper sample seating. The mineral samples were tested perpendicular to the cleavage plane of biotite and parallel to the C-direction of both quartz and albite. The temperature was measured by Type K thermocouples in contact with the samples' surface and the heating elements of the furnace. All samples were heated to temperatures of 20 ºC, 50 ºC, 100 ºC, 200 ºC, 300 ºC, and 400 ºC, and maintained for 24 hours at each temperature to allow thermal stabilization between the indenter tip and the sample surfaces.

After thermal stabilization was reached, mechanical tests including loading, creep, and unloading stages were performed. The loading stage lets the indenter establish contact and penetrate the sample's surface until it reaches a load of 100mN (i.e., 0.1N) while measuring the indenter's penetration depth. The creep stage measures the indenter's penetration while the load of 0.1N is held constant for 20 seconds. And the unloading stage reduces the load back to 0N. Both loading and unloading used a loading rate of 200mN/min. The same loading-creep-unloading testing conditions were repeated at least 50 times at each temperature for all tested samples.

2.2 Instrumented indentation

Indentation theory assumes that materials deform both elastically and plastically during loading, and any rebound during unloading is elastic [*Oliver and Pharr*, 2004; *Oliver and Pharr*, 1992]. Therefore, the material's response to a full indentation loading-unloading cycle can be used to calculate its mechanical and surface properties. In an indentation test, the measured secant elastic modulus must account for the contribution of both the indenter and the testing material to the elastic deformation at the contact. Thus, the indentation elastic modulus E is given by [*Oliver and Pharr*, 2004]:

$$E=\left(1-v_s^2\right)\left[\frac{1}{E_{eff}}-\frac{1-v_i^2}{E_i}\right]^{-1}, \tag{1}$$

where, E_i and v_i are the elastic modulus and the Poisson's ratio of the indenter, and v_s is the Poisson's ratio of the tested material. The effective elastic modulus E_{eff} is computed through:

$$E_{eff}=\left(\frac{\pi}{A_c}\right)^{1/2}\left(\frac{S}{2}\right), \tag{2}$$

where A_c and S are the contact area (between the indenter and the testing material) and the sample stiffness, respectively [*Oliver and Pharr*, 2004]. Note also that the stiffness *S* can be determined using a

power-law correlation of a segment from the unloading curve [*ASTM-E2546*, 2015]. This segment starts at the onset of unloading and progresses to approximately 50% to 90% of load removal, and the S value can be calculated by:

$$S = Bm\left(d_{max} - d_f\right)^{m-1}, \tag{3}$$

where d_{max} corresponds to the indenter's maximum penetration depth at maximum applied load; d_f is the final penetration depth after load removal; the parameters B, m and d_f are the best-fit constants for the unloading force P versus displacement d curve using the power-law expression:

$$P = B\left(d - d_f\right)^m. \tag{4}$$

Because the stiffness S is simply the change of load with respect to deformation, Equation (3) results from the derivative of Equation (4) with respect to the penetration depth [*ASTM-E2546-15*].

For a Berkovich indenter, which is used in this study, the contact area A_c in Equation (2) correlates with the contact height d_c as:

$$A_c = 24.5\, d_c^2. \tag{5}$$

Considering that the total height of penetration during load application does not represent full contact between the indenter and the testing material (some material surface around the indenter sinks in and separates from its faces as the indenter penetrates the sample), the contact height d_c is calculated as [*Joslin and Oliver*, 1989]:

$$d_c = d_{max} - 0.75\frac{P_{max}}{S}, \tag{6}$$

where P_{max} is the maximum applied load. Finally, the hardness H of the tested material is defined by the ratio of the maximum applied load to the contact area:

$$H = \frac{P_{max}}{A_c}\,. \tag{7}$$

2.3 Representative indentation data

Figure 1a shows the indentation curves for albite, quartz, and biotite loaded to 0.1N, creep at a constant load of 0.1N for 20 seconds, and unloaded to 0N. The maximum penetration depths for albite, quartz, and biotite are approximately 0.81 μm, 1.03 μm, and 1.86 μm (Figure 1a). Within 20 seconds of creep, biotite, quartz, and albite respectively show approximate maximum deformation depths of 76.9nm, 22.3nm, and 12.6nm (Figure 1b). The shaded areas under the creep curves of the tested minerals illustrate the transient creep with a deaccelerated deformation rate, while the straight lines indicate the steady-state creep where deformation rates become constant (Figure 1b). These indentation curves show that biotite

undergoes more deformation than quartz and albite both during the loading and the creep stages of indentation.

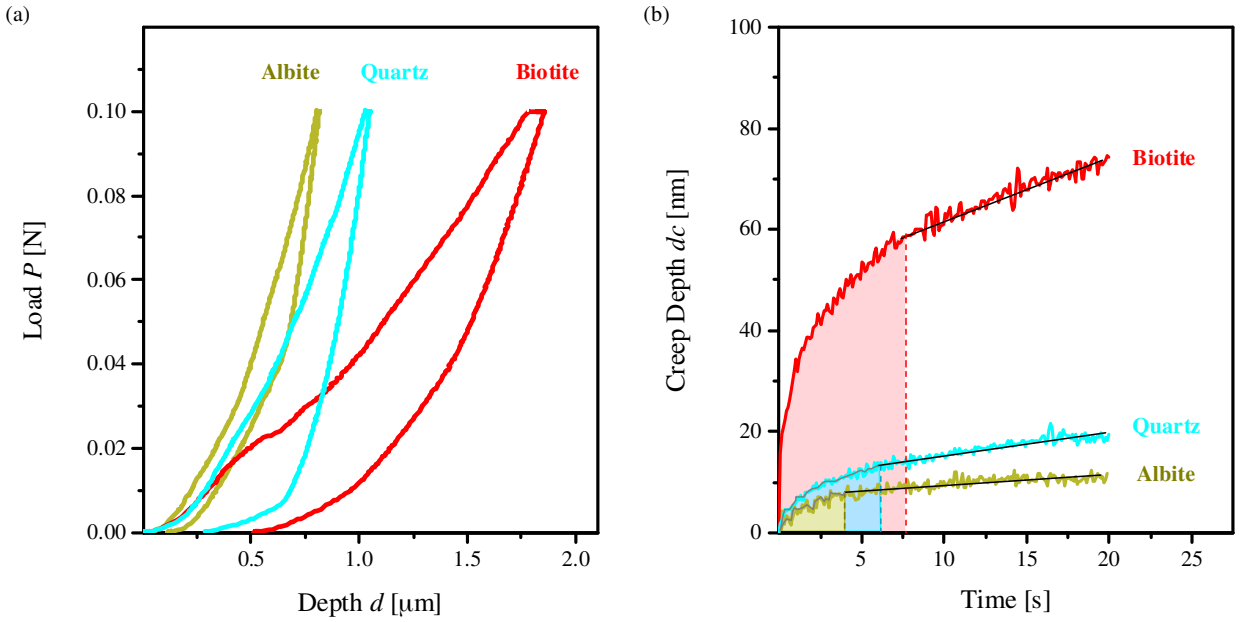

Figure 1. Indentation results for albite, quartz, and biotite at room temperature. (a) Load vs. penetration depth during loading, creep, and unloading stages. (b) Time-lapse creep deformation depth.

2.4 Experimental results

Indentation signatures of all tested albite, quartz, and biotite samples at temperatures ranging from 20 ⁰C to 400 ⁰C are shown in Figure 2. The maximum penetration depth for biotite d_{max} ~ 3.5μm is greater than those of albite d_{max} ~ 1.7μm and quartz d_{max} ~ 1.6μm at room temperature conditions (Figure 2). Additionally, the upper bounds of d_{max} for quartz and albite approximately align with the lower bound of d_{max} for biotite. The three tested minerals all show a tendency of increasing d_{max} with increasing temperature (Figure 2).

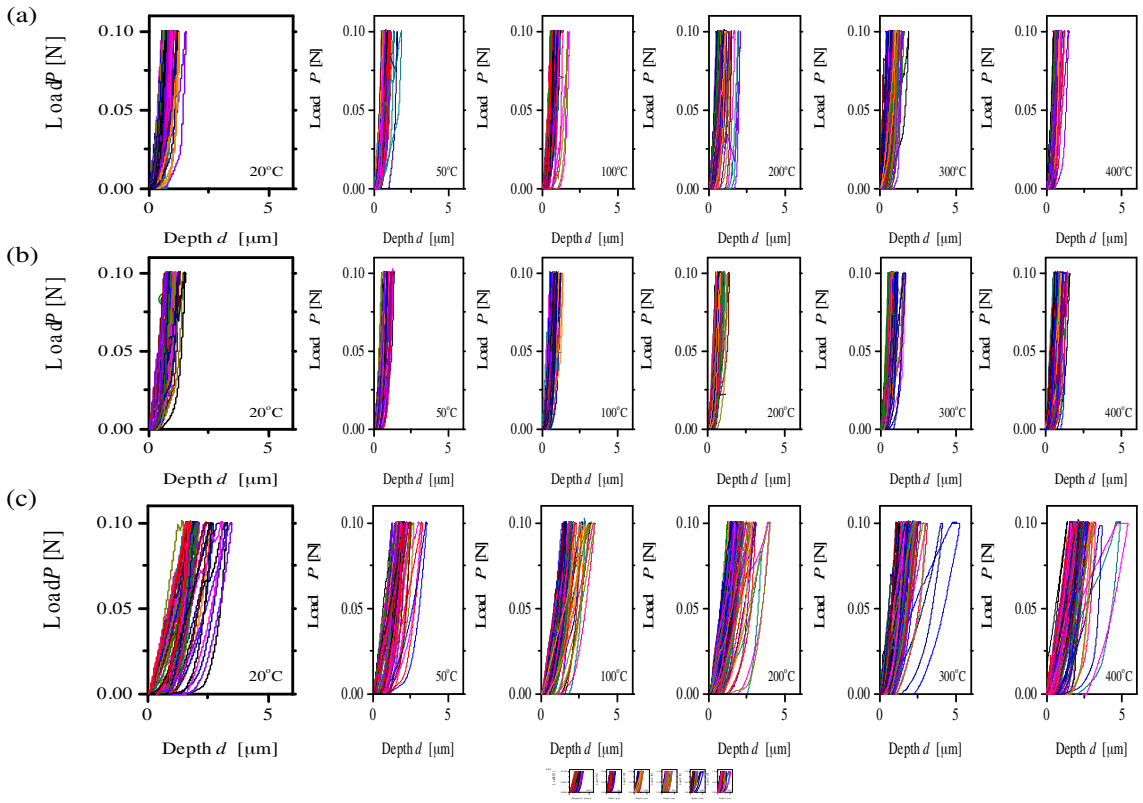

Figure 2. Indentation signatures of (a) albite, (b) quartz, and (c) biotite under various temperatures. Each temperature condition includes 50 indentations.

The creep deformation of all tested samples is summarized in Figure 3. At all tested temperatures, the creep deformation of biotite is the most pronounced. The maximum creep deformation within 20 seconds for albite, quartz, and biotite all increase with increasing temperature. Compared to that at room temperature, the maximum creep deformation within 20 seconds for albite, quartz, and biotite has increased by approximately two, five, and four fold at 400 ºC.

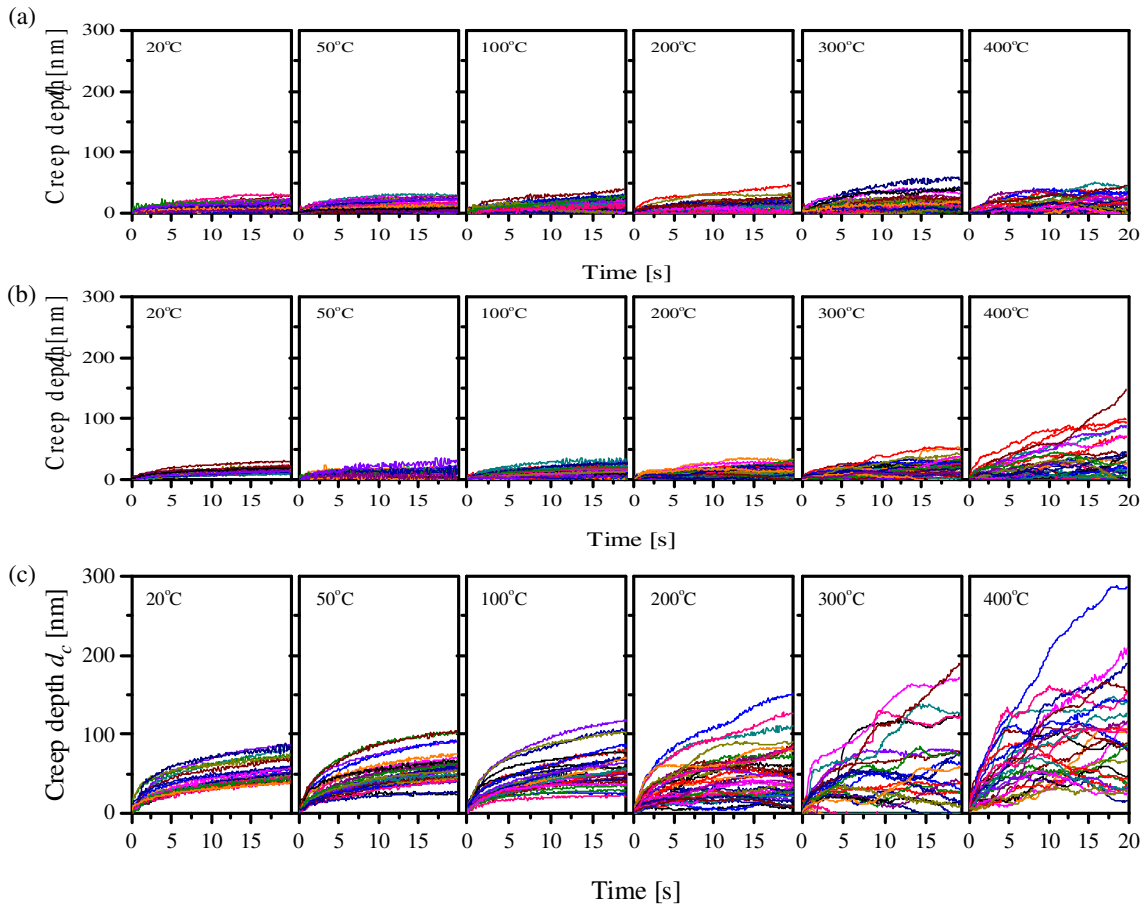

Figure 3. Creep deformation of (a) albite, (b) quartz, and (c) biotite tested at temperatures of 20 °C, 50 °C, 100 °C, 200 °C, 300 °C, and 400 °C. Each temperature condition includes 50 indentations.

3 Analyses and discussion

3.1 Elastic modulus with temperature

The elastic moduli of the three minerals at all tested temperatures were calculated from the unloading portion of the indentation curves presented in Figure 2 through Equation (1). Measured elastic moduli of all tested minerals soften as the temperature increases. The peaks of the modulus distributions shift towards the left especially at 400 °C, with standard deviations oscillating independent of temperature increase and with increasing coefficients of variation illustrating material softening with increasing temperature (Figure 4).

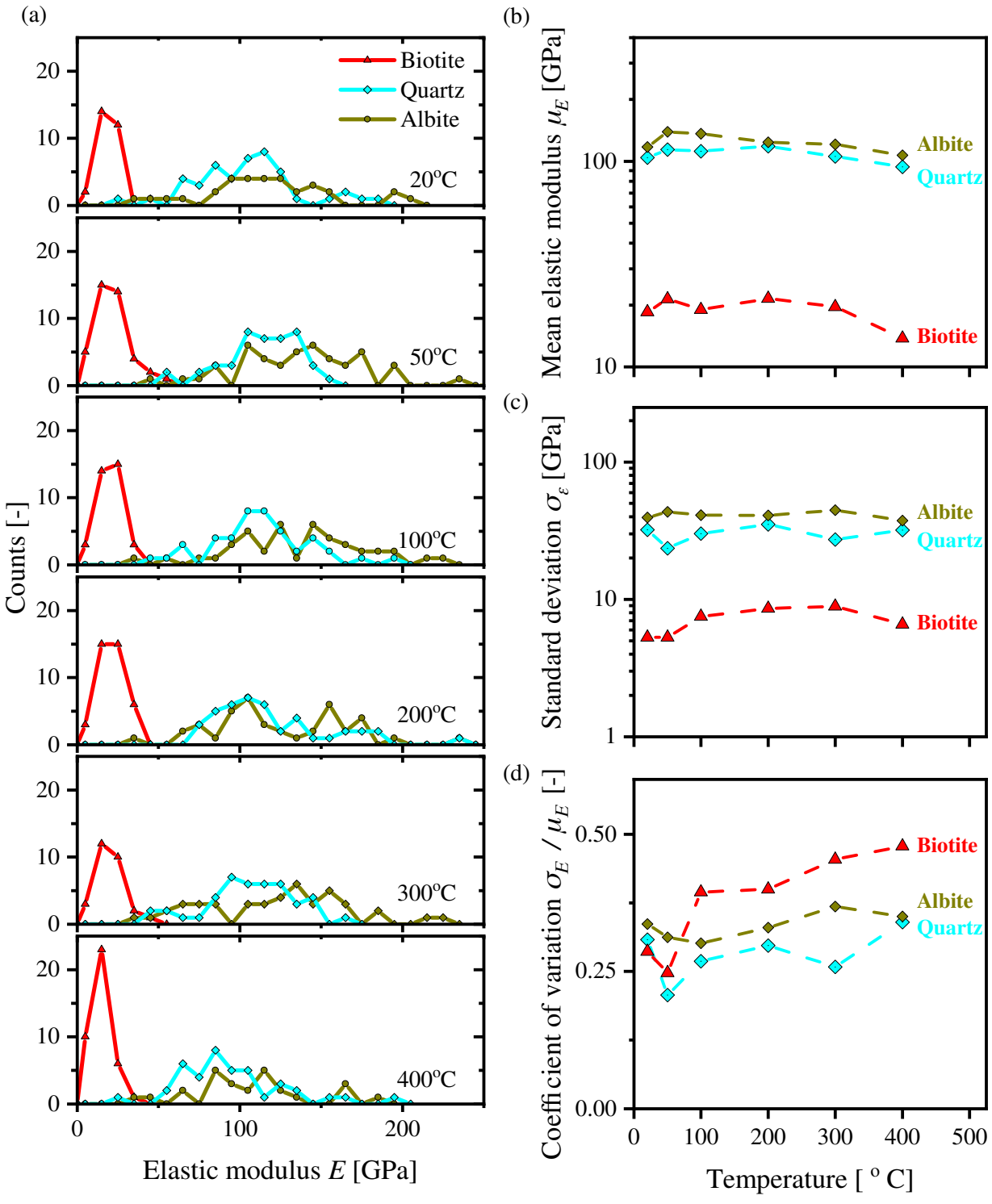

Figure 4. (a) Histograms, (b) means, (c) standard deviations, and (d) coefficients of variation of indentation elastic modulus for albite, quartz, and biotite at various temperatures.

Biotite has the lowest modulus compared to quartz and albite. The higher end of the moduli distribution for biotite approximately intersects the lower ends of the distributions for quartz and albite at all testing temperatures. At 400 ºC, the elastic modulus of biotite reduces by 25% compared with its room temperature condition, whereas those of quartz and albite reduce by approximately 10%. Therefore, biotite is not only the weakest of the three tested minerals but also the phase that might influence the possible weakening effects of granitic structures exposed to elevated temperatures.

The elastic modulus presented in Figure 4 suggests two competing effects of temperature in the mechanical response of tested minerals: strengthening due to thermal expansion caused by crack closure as well as softening due to thermal degradation resulting in softer minerals. The reduction of fracturing events during indentation (details in Section 3.3) as well as material dilation observed during testing suggest that, as temperature increases, fracture-closing mechanisms increase the material resistance to deformation under loading. This implies that the natural dislocations of pure minerals allow further compliance (deeper indenter penetration) at room temperature conditions than at high temperatures. The possible reduction of the internal spaces in fractures might have caused the transient increase in the elastic modulus of the tested minerals. This result is consistent with other studies that showed a rise in the elastic modulus of quartz and granites up to 300 °C, followed by a decrease at higher temperatures [*Trnik et al.*, 2019; *Yang et al.*, 2017].

3.2 Hardness with temperature

Obtained hardness for biotite is lower than that of albite and quartz at all tested temperature conditions, which further indicates the mechanical contrast between strong and weak mineral phases as manifested in elastic modulus measurements. The temperature-dependent hardness also slightly increases followed by decreasing trends with increased temperature, similar to their temperature-dependent elastic modulus responses. The hardness peaks at 200 ºC for quartz and at 300 ºC for biotite and albite; strong minerals show sharp hardness increments, at 50 ºC, in addition to their peaks (Figure 5).

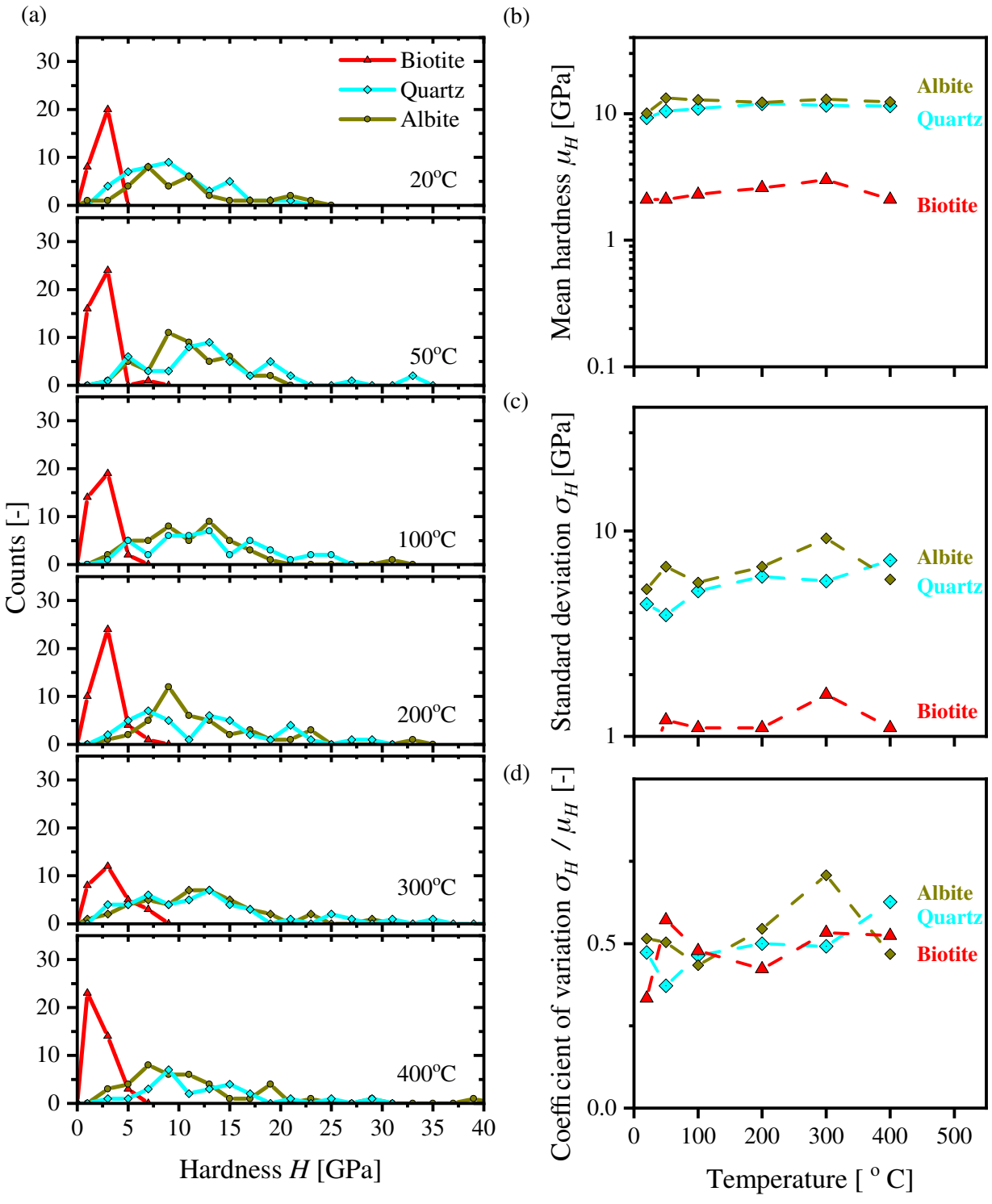

Figure 5. Histograms, (b) means, (c) standard deviations, and (d) coefficients of variation of indentation hardness for albite, quartz, and biotite at various temperatures.

3.3 Fracture behavior with temperature

The fracture toughness of tested minerals is evaluated using the energy analysis method [*Cheng et al.*, 2002; *Liu et al.*, 2016]. The fracture toughness K_c is calculated by:

$$K_c = \sqrt{G_c E}\ , \tag{8}$$

where G_c is the critical energy release rate calculated by the ratio of fracture energy U_{crack} to the maximum contact area A_{c-max}. The former is calculated from the portion of fracturing energy comprised within the area in between the loading and unloading stages of indentation curves (see details in the Appendix), and the latter from Equation (5) using the maximum value of d_c. The elastic modulus E is calculated using Equation (1).

The results using this method show that fracture toughness slightly increases with increasing temperature for all tested minerals, with quartz showing the most pronounced fracture toughness increase upon heating (Figure 6a). Fracture toughness quantitatively describes a material's resistance to crack propagation, and materials with high fracture toughness tend to behave more ductile at failure. The ductility increase and decay in biotite and albite at elevated temperatures could respond to a combination of sequential crack healing and crack generation processes and material softening. The transition from increasing to decreasing fracture toughness has also been evidenced in other studies testing individual minerals [*Darot et al.*, 1985] and granites [*Feng et al.*, 2019; *Hu et al.*, 2018] [*Meredith and Atkinson*, 1985] at similar temperatures.

Figure 6b shows an indentation curve that suffered a pop-in event, i.e., a sudden displacement burst typically associated with a fracture or crack initiation and propagation [*Bor et al.*, 2019]. This pop-in event occurred at a failure load P_f ~0.055N with a length of a ~0.25μm when the penetration depth is approximately at d ~0.7μm. Note that the hardness and elastic modulus data presented in previous sections are all based on indentation tests with no pop-in events. Except for quartz at 100 ºC and 400 ºC, and albite at 400 ºC, all other samples showed pop-in events (Figure 6c).

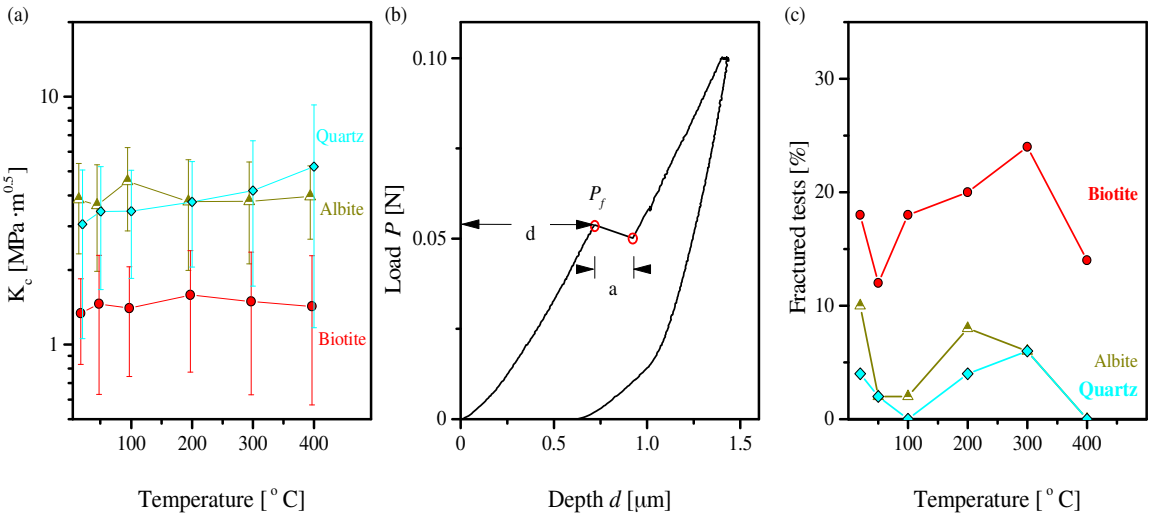

Figure 6. Fracture responses. (a) Calculated fracture toughness using the energy analysis method. (b) Typical pop-in event during loading. (c) Percentage of fractured tests (i.e. comprising at least one pop-in event) during loading.

Below 100ºC, increased temperature enhances the modulus and hardness of tested minerals (as discussed in previous sections) and slightly reduces the occurrence of pop-in events during indentation (Figure 6c). Overall, biotite evidently presents more fracture susceptibility than quartz and albite, suggesting a higher likelihood of brittle failure in the biotite phase in granitic composites, particularly at elevated temperature conditions. Hence, it can be inferred that fracture generation might be more prominent in granitic composites with high biotite contents than in granitic composites with high content of quartz and albite. Thermal expansion contrast between biotite, quartz, and albite have been shown to induce stress concentration leading to fracturing mechanisms in granites [*Vázquez et al.*, 2015]. Mineral orientation and rock texture also contribute to thermal fracturing [*Siegesmund et al.*, 2008].

3.4 Maximum creep deformation with temperature

During the 20-second creep stage, the total creep deformation for biotite increased from an average of 58.9nm at 20 ºC to 125.7nm at 400 ºC (Figure 7). Below 300 ºC, the creep deformation increased slightly with increased temperature, and a more pronounced creep deformation with a higher variance was developed at 400ºC. While temperature has less influence on the creep deformation of albite and quartz, their maximum creep deformation remained nearly unchanged up to 300 ºC, and then slightly increased at 400 ºC. The creep deformation for these minerals could respond to mechanisms such as dislocation creep

[*Fukuda and Shimizu*, 2017], competing dislocations systems that transition from basal dislocations to prism dislocation glide [*Lister*, 1981] or crystal lattice rotation [*Takeshita and Wenk*, 1988], and can be exacerbated by high-temperature conditions.

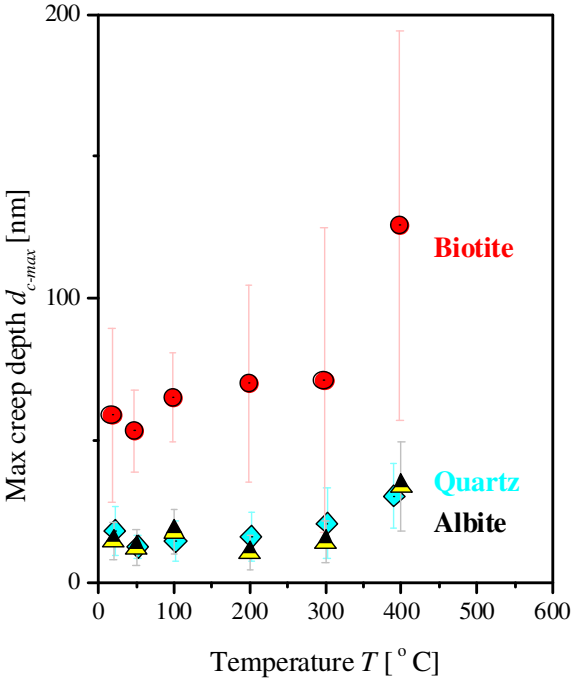

Figure 7. Temperature-dependent maximum creep deformation (within 20 seconds) for biotite, quartz, and albite.

Under the same temperature, the creep deformation in biotite is about 3-4 times that in quartz and albite. Such mismatch in creep deformation enlarges at higher temperature conditions. This attributes to the structural difference of tested minerals, as biotite can undergo more exacerbated deformation upon heating than the other two minerals, due to smaller elastic modulus and its characteristic one-dimensional cleavage, which undergoes ripplocations (layer ripples at the atomic level) and the formation of kink bands on their basal planes [*Anderson*, 1987; *Barsoum*, 2020; *Etheridge et al.*, 1973]. Additionally, biotite structures exposed to temperatures up to 400 ºC have shown axial elongation and separation of their interlayer bonds in the c-direction [*Chon et al.*, 2003]. Such a mismatch in creep deformation among different granitic minerals can contribute to long-term granite damage due to temperature change.

3.5 Time-lapse creep analysis

Using the traditional unidimensional models to characterize the primary and the secondary creep [*Lomnitz*, 1956; *Vandamme and Ulm*, 2009], we here describe the indentation creep deformation, $d_c(t)$ [nm] following a logarithmic law with respect to time t [s] through:

$$d_c(t) = X_1 \cdot \ln(X_2 \cdot t + 1) + X_3 \cdot t \,, \tag{9}$$

where X_1 [nm] is a material constant describing the overall magnitude of the primary creep deformation; X_2 [1/s] is the characteristic rate of primary creep, the reciprocal of which reflects the duration of primary creep; and X_3 [nm/s] characterizes the creep rate of the secondary (i.e., constant) creep. The illustration and impacts of fitting constants X_1, X_2, and X_3 on the creep deformation behavior are shown in Figure 8.

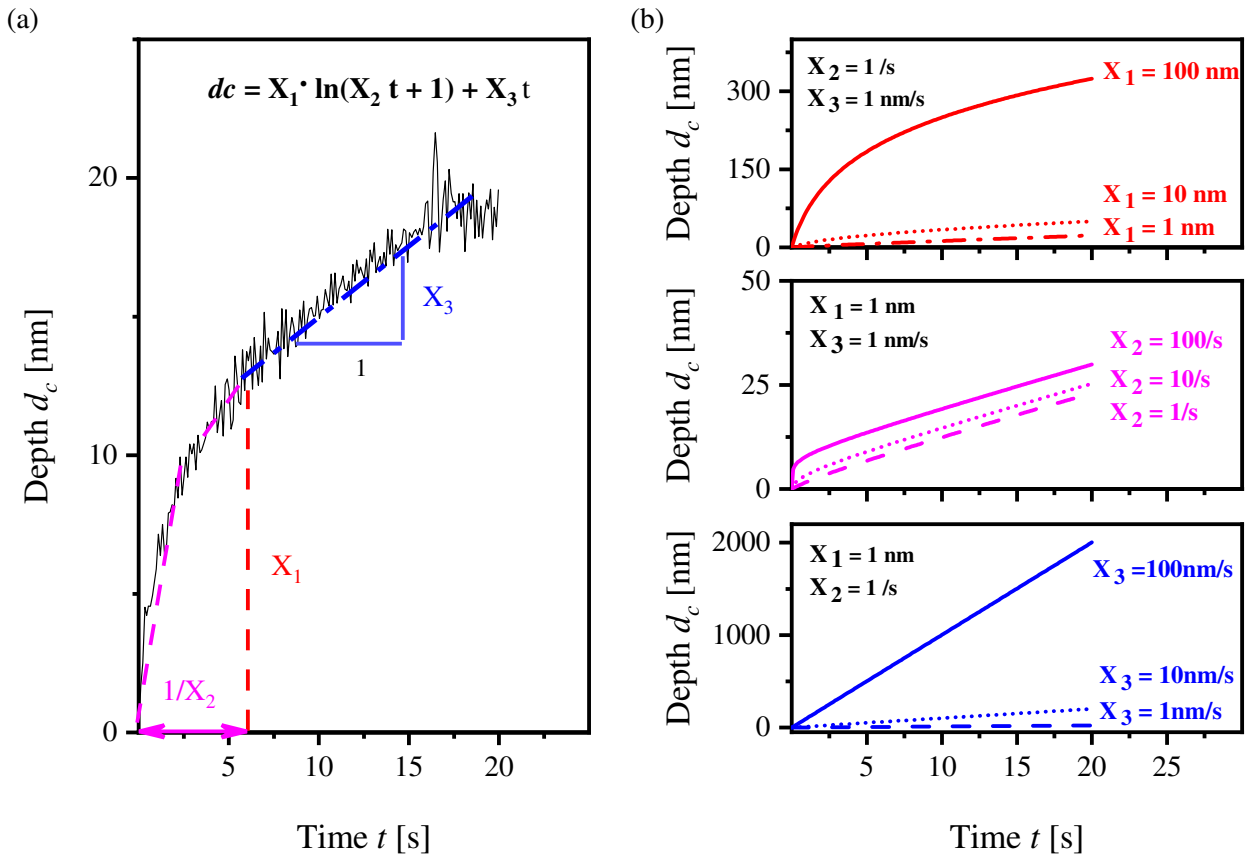

Figure 8. Indentation creep deformation. (a) The time-dependent creep deformation is captured using a three-parameter creep model. (b) Creep deformation was calculated with unitary, tenfold, and hundredfold values of the constants X_1 [nm], X_2 [1/s], and X_3 [nm/s] to illustrate their control of the creep behavior.

The magnitude of primary creep X_1 increases exponentially with temperature for all tested samples (Figure 9a), with the magnitude for biotite about one order of magnitude larger than that for albite and

quartz. The characteristic rate of primary creep X_2 decreases with increasing temperature for albite and quartz (Figure 9b), suggesting longer primary creep duration, i.e., a more viscous and ductile response at elevated temperatures. In contrast, the X_2 for biotite increases exponentially with increasing temperature (Figure 9b), presenting less viscous and more brittle deformation behaviors at a higher temperature.

While elevated temperature causes biotite to accelerate its onset of steady-state creep, it causes the opposite effect on albite and quartz. Such divergent behavior might result from the interaction of competing deformation mechanisms typical of crystalline minerals including inter-grain space reduction through grain dilation, generation of intra-grain vacancies, grain boundary rotation, and grain sliding [*Soda et al.*, 2019]. Additionally, basal dislocation is the main deformation mechanism of biotite at high temperatures [*Etheridge et al.*, 1973]. Hence, the deformation of divergent nature among minerals might extend the transient creep time of quartz and albite but shorten that of biotite. Creep deformation triggered by thermally induced dislocations generated by the large coefficient of thermal expansion of biotite could also cause the increasing behavior of constant X_2 (i.e., the reduction of transient creep time). At 400 ºC, the three tested minerals show almost identical transient creep duration.

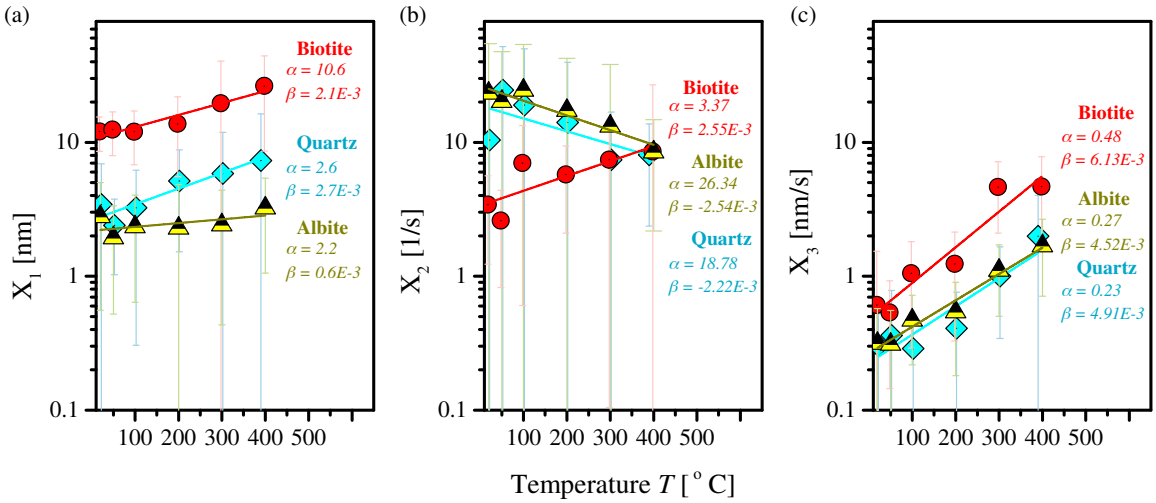

Figure 9. Creep model parameter values of (a) primary creep magnitude X_1 [nm], (b) the reciprocal of primary creep duration X_2 [1/s], (c) the rate of secondary creep X_3 [nm/s] with temperature *T*. Data are fitted by $X_i = \alpha e^{\beta T}$, where *i* = 1, 2, and 3; α and β are fitting parameters listed in the plots.

As shown in Figure 9c, with the increase of temperature from 20 ºC to 400 ºC, all tested minerals show an exponentially increased rate of secondary creep, i.e., constant X_3. Albite and quartz have almost identical secondary creep rates at all tested temperatures, which are about one-third to half of that of biotite at the

same temperature. Hence, despite the increasing rate of deformation of all minerals during secondary creep, biotite shows the largest susceptibility to thermal damage and it is likely to aggravate the rate of deformation on biotite-rich granite composites.

Note that the large creep deformation in biotite at high temperatures (Figure 7) is mainly because both the magnitude of initial deformation (X_1) and the rate of secondary deformation (X_3) exponentially increase with temperature, and the values of X_1 and X_3 for biotite are about one order of magnitude larger than that for albite and quartz, as shown in Figure 9. On the other hand, phase transformation will not be a cause of the creep deformation in this study. At atmospheric pressure, the phase transformation for albite and quartz starts at temperatures of 1080°C [*Winter et al.*, 1979] and 573°C [*Ohno et al.*, 2006] respectively, both of which are higher than the tested temperature in this study (up to 400°C). Tested temperatures up to 400°C cannot induce phase transformation for biotite either. However, biotite is of highly perfect basal cleavage and consists of flexible sheets or lamellae that can easily flake off. With increasing in temperature, there will be additional shrinkage in both the sheet thickness and the interlayer separation [*Chon et al.*, 2003], which exacerbates the creep deformation.

In addition, although the same load of 100mN was applied during creep for all three tested minerals, the stress level may be different due to different penetration depths (or indentor-material contact areas). The stress level during creep can be calculated as a function of the maximum applied load P_{max} and the maximum penetration depth d_{max} through:

$$\sigma = \frac{P_{max}}{24.5 \cdot d_{max}^{\,2}} . \qquad (10)$$

The result in Figure 10 shows that the creep deformation in biotite was measured under a stress level approximately five times smaller than the other two minerals, due to the larger contact area in biotite under identical indentation force. Therefore, at identical stress levels as albite and quartz, a larger creep deformation in biotite is expected. The rise and subsequent decline of stress during the creep phase also shows both the contact area reduction related to fracture-closure(strengthening) mechanisms and the material softening of all tested minerals at elevated temperatures.

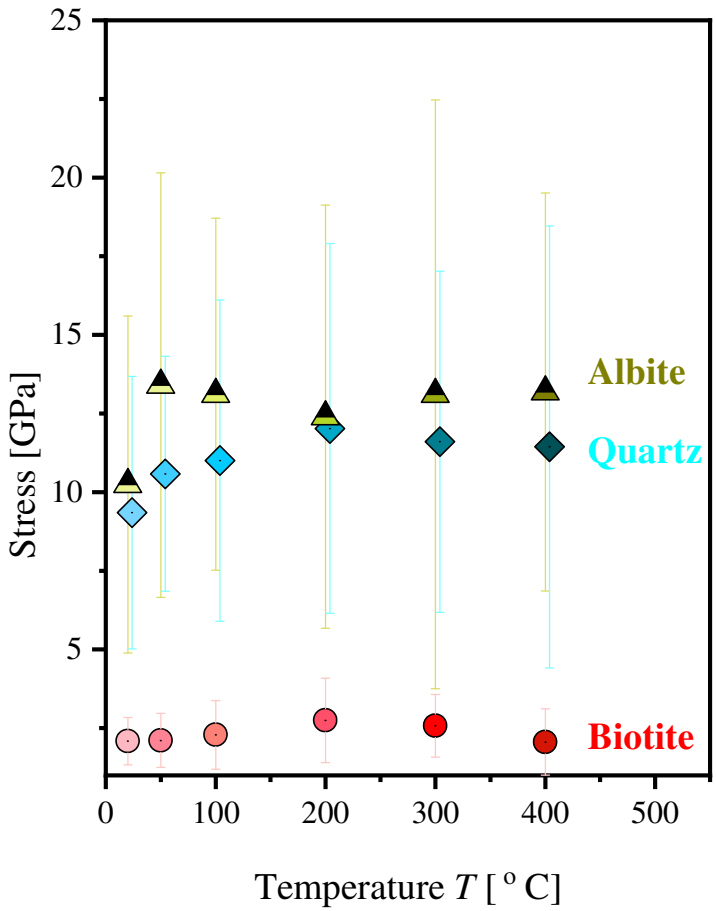

Figure 10. The stress and strain rate of albite, quartz, and biotite during the creep deformation at all tested temperatures.

3.6 Creep constants and elastic modulus

With increased temperature, all minerals show an evident reduction of elastic modulus and an increased transient creep deformation expressed through X_1. The magnitude of transient creep X_1 is inversely proportional to the elastic modulus E in logarithmic scales for the three minerals at all tested temperatures, as shown in Figure 11a. This relation can be well described by an empirical relation of X_1[nm] = 400/E[GPa]. This agreement implies that the transient creep of granitic minerals can be predicted using their elastic moduli for all temperatures. The observed material softening could be attributed to degradation mechanisms including the growth of intergranular and intragranular dislocations, preferential grain boundary sliding, and heterogeneous mineral expansion [*Ashby*, 1972; *Hansen et al.*, 2011; *Warren and Hirth*, 2006]. Additionally, the rate of constant/secondary creep X_3 is proportional to the magnitude of primary creep X_1 logarithmically (Figure 11b). These relations provide quick estimates of the temperature-dependent creep behavior of granitic minerals using their elastic properties at elevated temperatures, especially when those creep constants are not readily available.

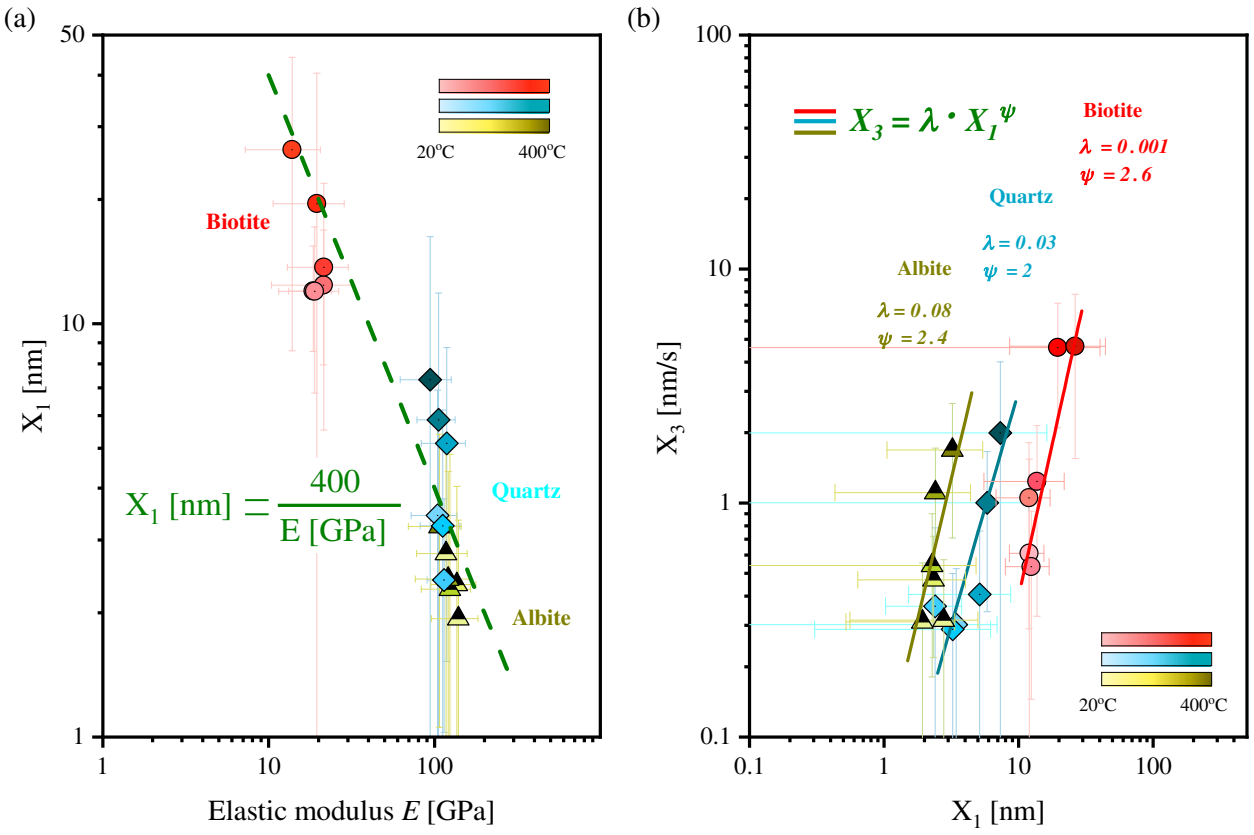

Figure 11. Creep constants and elastic modulus. (a) The primary creep depth X_1 [nm] is inversely proportional to the elastic modulus E of biotite, albite, and quartz at all tested temperatures in a logarithmic scale. (b) The relationship between the primary creep depth X_1[nm] and the secondary creep rate X_3[nm/s] for albite, quartz, and biotite.

4 Conclusions

Minerals of albite, biotite, and quartz, typically comprising granitic rocks, were tested at temperatures up to 400 °C using an instrumented indentation device in this study. Major conclusions include:

- Quartz and albite show a mechanical contrast with respect to biotite. The room temperature elastic moduli of albite (117.4GPa) and quartz (104.3GPa) are at least five times greater than that of biotite (18.5 GPa). At elevated temperatures, biotite undergoes greater mechanical degradation than quartz and albite. The elastic modulus of biotite reduces by 25%, whereas the elastic modulus of quartz and albite respectively reduce by 9.7% and 8.7%.
- Granitic rocks with high biotite content will compromise the most with increasing temperature, as biotite is not only the weakest mineral phase but also the one showing the most thermal degradation. Elevated temperature tends to increase the fracture toughness of quartz and albite due to more ductile behavior evidenced by the reduced number of fracturing events during loading, while biotite presents a higher likelihood of brittle failure (i.e., pop-in events) during indentation loading, particularly at elevated temperature conditions.
- The temperature increase from 20 ºC to 400 ºC caused a two-fold increment in the creep deformation within 20 seconds for albite, quartz, and biotite. Biotite showed at least three times the overall creep deformation compared to quartz and albite under the same temperature.
- The indentation creep deformation in the tested minerals can be characterized using a logarithmic function of time. Such a logarithmic approach allows the estimation of the characteristic creep depth and characteristic time of transient creep.
- The transition from transient creep to steady-state creep for biotite is approximately three times faster than those of albite and quartz, possibly due to its sheet-like structure with an abundance of interfacial spacings that facilitate material deformation, especially at elevated temperatures.
- Transient creep accounts for the majority of the total creep deformation and steady-state creep plays a minor role within the 20 seconds creep measurement. However, over a longer time, the secondary creep deformation can continue to develop at a constant rate resulting in large deformation until failure. The rate of secondary creep for biotite is about three times that of albite and quartz at the same temperature. As temperature increases from 20 ºC to 400 ºC, the rate of secondary creep escalates about 10 times faster.

- The deformation of transient creep and the rate of secondary creep can be empirically correlated to the elastic moduli of albite, biotite, and quartz. These relations allow quick estimates of the temperature-dependent creep behavior of granitic minerals using their elastic properties, especially when those creep constants are not readily available at elevated temperatures.

Appendix. Energy method to estimate fracture toughness

The total energy W_{tot} used in the penetration process of an indenter into a testing sample corresponds to the area under the indentation loading curve. Such energy consists in an elastic portion W_e that corresponds to the sample's rebound under unloading conditions and the plastic portion W_p corresponding to an irrecoverable phase of materials caused by internal instabilities preventing further elastic deformation during unloading (Figure A-12).

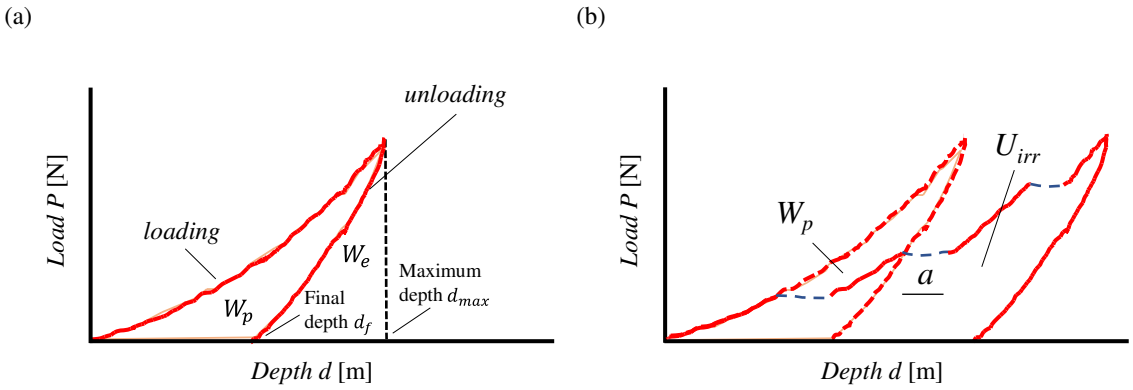

Figure A-12 Indentation energy in a loading-unloading cycle. (a) Total energy distributed in elastic energy W_e during material unloading rebound and plastic energy W_p caused by plastic mechanisms excluding major cracking events. (b) Plastic energy W_p and irrecoverable energy U_{irr} including cracking events of approximate length a.

The plastic energy W_p can be calculated from the proportionality between the ratio of the plastic energy W_p to the total energy W_{tot} with the ratio of the final penetration depth d_f to the maximum penetration depth d_{max} through [*Cheng et al.*, 2002]:

$$\frac{W_p}{W_{tot}} = 1 - \left\{ \frac{1 - 3\left(\frac{d_f}{d_{max}}\right)^2 + 2\left(\frac{d_f}{d_{max}}\right)^3}{1 - \left(\frac{d_f}{d_{max}}\right)^2} \right\} \tag{A.1}$$

The energy used for crack generation U_{crack} is estimated from the irrecoverable energy U_{irr} that combines plastic mechanisms associated with material rearrangement and fracturing events using [*Liu et al.*, 2016]:

$$U_{crack} = U_{irr} - W_p \tag{A.2}$$

The critical energy release rate is measured as a ratio of the energy for crack generation U_{crack} to the maximum contact area A_{c-max} by:

$$G_c = \frac{U_{crack}}{A_{c-max}} \tag{A.3}$$

The fracture toughness is calculated by [*Liu et al.*, 2016]:

$$K_c = \sqrt{G_c E} \tag{A.4}$$

Acknowledgement

This material is based upon work supported by the National Science Foundation (EEC-1449501, CMMI-1943722, CMMI-2134311, and IRES-1854030). Any opinions, findings and conclusions, or recommendations expressed in this material are those of the authors and do not necessarily reflect those of the NSF. This study also benefited from the discussions with Dr. Chloe Arson (Georgia Institute of Technology) and Dr. Matthieu Vandamme (Ecole des Ponts, Paris Tech).

References

Anderson, T. B. (1987), KINK BANDSKink bands, in *Structural Geology and Tectonics*, edited, pp. 373-377, Springer Berlin Heidelberg, Berlin, Heidelberg, doi:10.1007/3-540-31080-0_58.

Ashby, M. F. (1972), A first report on deformation-mechanism maps, *Acta Metallurgica*, *20*(7), 887-897, doi:https://doi.org/10.1016/0001-6160(72)90082-X.

ASTM-E2546-15 Standard Practice for Instrumented Indentation Testing, in *ASTM International*, edited.

ASTM-E2546 (2015), Standard Practice for Instrumented Indentation Testing, in *ASTM International*, edited.

Barsoum, M. W. (2020), Ripplocations: A Progress Report, *Frontiers in Materials*, *7*(146), doi:10.3389/fmats.2020.00146.

Bor, B., D. Giuntini, B. Domènech, M. V. Swain, and G. A. Schneider (2019), Nanoindentation-based study of the mechanical behavior of bulk supercrystalline ceramic-organic nanocomposites, *Journal of the European Ceramic Society*, *39*(10), 3247-3256.

Brinson, L. C., and T. S. Gates (1995), Effects of physical aging on long term creep of polymers and polymer matrix composites, *International Journal of Solids and Structures*, *32*(6-7), 827-846.

Cannon, W. R., and T. G. Langdon (1983), Creep of ceramics, *Journal of Materials Science*, *18*(1), 1-50.

Cheng, Y.-T., Z. Li, and C.-M. Cheng (2002), Scaling relationships for indentation measurements, *Philosophical Magazine A*, *82*(10), 1821-1829, doi:10.1080/01418610208235693.

Chon, C.-M., S. Kim, and H.-S. Moon (2003), Crystal Structures of Biotite At High Temperatures and of Heat-treated Biotite Using Neutron Powder Diffraction, *Clays and Clay Minerals - CLAYS CLAY MINER*, *51*, 519-528, doi:10.1346/CCMN.2003.0510506.

Cristescu, N. (2012), *Rock rheology*, Springer Science & Business Media.

Cristescu, N., and U. Hunsche (1998), *Time effects in rock mechanics*, Wiley New York.

Darot, M., Y. Gueguen, Z. Benchemam, and R. Gaboriaud (1985), Ductile-brittle transition investigated by micro-indentation: results for quartz and olivine, *Physics of the Earth and Planetary Interiors*, *40*(3), 180-186, doi:https://doi.org/10.1016/0031-9201(85)90128-1.

Etheridge, M. A., B. E. Hobbs, and M. S. Paterson (1973), Experiental deformation of single crystals of biotite, *Contributions to Mineralogy and Petrology*, *38*(1), 21-36, doi:10.1007/BF00371724.

Evans, R. W., and B. Wilshire (1985), Creep of metals and alloys.

Fabre, G., and F. Pellet (2006), Creep and time-dependent damage in argillaceous rocks, *International Journal of Rock Mechanics and Mining Sciences*, *43*(6), 950-960, doi:https://doi.org/10.1016/j.ijrmms.2006.02.004.

Fei, W., L. Jie, Z. Quanle, L. Cunbao, C. Jie, and G. Renbo (2021), A triaxial creep model for salt rocks based on variable-order fractional derivative, *Mechanics of Time-Dependent Materials*, *25*(1), 101-118.

Feng, G., Y. Kang, and X.-C. Wang (2019), Fracture failure of granite after varied durations of thermal treatment: an experimental study, *R Soc Open Sci*, *6*(7), 190144-190144, doi:10.1098/rsos.190144.

Firme, P. A., N. B. Brandao, D. Roehl, and C. Romanel (2018), Enhanced double-mechanism creep laws for salt rocks, *Acta Geotechnica*, *13*(6), 1329-1340.

Firme, P. A., D. Roehl, and C. Romanel (2016), An assessment of the creep behaviour of Brazilian salt rocks using the multi-mechanism deformation model, *Acta Geotechnica*, *11*(6), 1445-1463.

Fujii, Y., T. Kiyama, Y. Ishijima, and J. Kodama (1999), Circumferential strain behavior during creep tests of brittle rocks, *International Journal of Rock Mechanics and Mining Sciences*, *36*(3), 323-337, doi:https://doi.org/10.1016/S0148-9062(99)00024-8.

Fukuda, J.-i., and I. Shimizu (2017), Theoretical derivation of flow laws for quartz dislocation creep: Comparisons with experimental creep data and extrapolation to natural conditions using water fugacity corrections, *Journal of Geophysical Research: Solid Earth*, *122*(8), 5956-5971, doi:https://doi.org/10.1002/2016JB013798.

Ghazvinian, E., M. S. Diederichs, and R. Quey (2014), 3D random Voronoi grain-based models for simulation of brittle rock damage and fabric-guided micro-fracturing, *Journal of Rock*

Mechanics and Geotechnical Engineering, *6*(6), 506-521, doi:https://doi.org/10.1016/j.jrmge.2014.09.001.

Goldsby, D. L., A. Rar, G. M. Pharr, and T. E. Tullis (2004), Nanoindentation creep of quartz, with implications for rate-and state-variable friction laws relevant to earthquake mechanics, *Journal of materials research*, *19*(1), 357-365.

Gratier, J.-P., R. Guiguet, F. Renard, L. Jenatton, and D. Bernard (2009), A pressure solution creep law for quartz from indentation experiments, *Journal of Geophysical Research: Solid Earth*, *114*(B3), doi:https://doi.org/10.1029/2008JB005652.

Griggs, D. (1939), Creep of rocks, *The Journal of Geology*, *47*(3), 225-251.

Hansen, L. N., M. E. Zimmerman, and D. L. Kohlstedt (2011), Grain boundary sliding in San Carlos olivine: Flow law parameters and crystallographic-preferred orientation, *Journal of Geophysical Research: Solid Earth*, *116*(B8), doi:https://doi.org/10.1029/2011JB008220.

Hu, J., Q. Sun, and X. Pan (2018), Variation of mechanical properties of granite after high-temperature treatment, *Arabian Journal of Geosciences*, *11*(2), 43, doi:10.1007/s12517-018-3395-8.

Joslin, D. L., and W. C. Oliver (1989), A new method for analyzing data from continuous depth-sensing microindentation tests, *Journal of Materials Research*, *5*(01), 123-126, doi:10.1557/jmr.1990.0123.

Kassner, M. E. (2015), *Fundamentals of creep in metals and alloys*, Butterworth-Heinemann.

Kranz, R. L. (1980), The effects of confining pressure and stress difference on static fatigue of granite, *Journal of Geophysical Research: Solid Earth*, *85*(B4), 1854-1866, doi:10.1029/JB085iB04p01854.

Kranz, R. L., and C. H. Scholz (1977), Critical dilatant volume of rocks at the onset of Tertiary creep, *Journal of Geophysical Research (1896-1977)*, *82*(30), 4893-4898, doi:10.1029/JB082i030p04893.

Lin, Q. X., Y. M. Liu, L. G. Tham, C. A. Tang, P. K. K. Lee, and J. Wang (2009), Time-dependent strength degradation of granite, *International Journal of Rock Mechanics and Mining Sciences*, *46*(7), 1103-1114, doi:https://doi.org/10.1016/j.ijrmms.2009.07.005.

Lister, G. S. (1981), The effect of the basal-prism mechanism switch on fabric development during plastic deformation of quartzite, *Journal of Structural Geology*, *3*(1), 67-75, doi:https://doi.org/10.1016/0191-8141(81)90057-2.

Liu, K., M. Ostadhassan, and B. Bubach (2016), Applications of nano-indentation methods to estimate nanoscale mechanical properties of shale reservoir rocks, *Journal of Natural Gas Science and Engineering*, *35*, 1310-1319, doi:https://doi.org/10.1016/j.jngse.2016.09.068.

Liu, Q., Y. Jiang, Z. Wu, and J. He (2018), A Voronoi element based-numerical manifold method (VE-NMM) for investigating micro/macro-mechanical properties of intact rocks, *Engineering Fracture Mechanics*, *199*, 71-85, doi:https://doi.org/10.1016/j.engfracmech.2018.05.010.

Lockner, D. (1993), Room temperature creep in saturated granite, *Journal of Geophysical Research: Solid Earth*, *98*(B1), 475-487.

Lomnitz, C. (1956), Creep measurements in igneous rocks, *The Journal of Geology*, *64*(5), 473-479.

Masuda, K., H. Mizutani, and I. Yamada (1987), EXPERIMENTAL STUDY OF STRAIN-RATE DEPENDENCE AND PRESSURE DEPENDENCE OF FAILURE PROPERTIES OF GRANITE, *Journal of Physics of the Earth*, *35*(1), 37-66, doi:10.4294/jpe1952.35.37.

Masuda, K., H. Mizutani, I. Yamada, and Y. Imanishi (1988), EFFECTS OF WATER ON TIME-DEPENDENT BEHAVIOR OF GRANITE, *Journal of Physics of the Earth*, *36*(6), 291-313, doi:10.4294/jpe1952.36.291.

Meredith, P. G., and B. K. Atkinson (1985), Fracture toughness and subcritical crack growth during high-temperature tensile deformation of Westerly granite and Black gabbro, *Physics of the Earth and Planetary Interiors*, *39*(1), 33-51, doi:https://doi.org/10.1016/0031-9201(85)90113-X.

Ohno, I., K. Harada, and C. Yoshitomi (2006), Temperature variation of elastic constants of quartz across the α-β transition, *Physics and Chemistry of Minerals*, *33*, 1-9.

Oliver, and G. Pharr (2004), Measurement of hardness and elastic modulus by instrumented indentation: Advances in understanding and refinements to methodology, *Journal of Materials Research*, *19*(1), 3-20.

Oliver, W. C., and G. M. Pharr (1992), An improved technique for determining hardness and elastic modulus using load and displacement sensing indentation experiments, *Journal of Materials Research*, *7*(6), 1564-1583, doi:10.1557/JMR.1992.1564.

Perzyna, P. (1966), Fundamental Problems in Viscoplasticity, in *Advances in Applied Mechanics*, edited by G. G. Chernyi, H. L. Dryden, P. Germain, L. Howarth, W. Olszak, W. Prager, R. F. Probstein and H. Ziegler, pp. 243-377, Elsevier, doi:https://doi.org/10.1016/S0065-2156(08)70009-7.

Siegesmund, S., S. Mosch, C. Scheffzük, and D. I. Nikolayev (2008), The bowing potential of granitic rocks: rock fabrics, thermal properties and residual strain, *Environmental Geology*, *55*(7), 1437-1448, doi:10.1007/s00254-007-1094-y.

Soda, Y., Y. Harigane, K. Kajimoto, and T. Okudaira (2019), Crystallographic preferred orientations of plagioclase via grain boundary sliding in a lower-crustal anorthositic ultramylonite, *International Journal of Earth Sciences*, *108*(6), 2057-2069, doi:10.1007/s00531-019-01749-z.

Sorelli, L., G. Constantinides, F.-J. Ulm, and F. Toutlemonde (2008), The nano-mechanical signature of ultra high performance concrete by statistical nanoindentation techniques, *Cement and Concrete Research*, *38*(12), 1447-1456.

Sun, C., G. Li, M. E. Gomah, J. Xu, and Y. Sun (2020), Creep characteristics of coal and rock investigated by nanoindentation, *International Journal of Mining Science and Technology*, *30*(6), 769-776, doi:https://doi.org/10.1016/j.ijmst.2020.08.001.

Takeshita, T., and H.-R. Wenk (1988), Plastic anisotropy and geometrical hardening in quartzites, *Tectonophysics*, *149*(3), 345-361, doi:https://doi.org/10.1016/0040-1951(88)90183-7.

Trnik, A., I. Stubna, J. Ondruška, P. Sin, and C. Štefan (2019), Young's modulus of prefired quartz porcelain in a temperature range of 20–1200 °C, *Materiali in tehnologije*, *53*, 535-541, doi:10.17222/mit.2018.252.

Urai, J. L., C. J. Spiers, H. J. Zwart, and G. S. Lister (1986), Weakening of rock salt by water during long-term creep, *Nature*, *324*(6097), 554-557.

Vandamme, M., and F.-J. Ulm (2009), Nanogranular origin of concrete creep, *Proceedings of the National Academy of Sciences*, *106*(26), 10552, doi:10.1073/pnas.0901033106.

Vázquez, P., V. Shushakova, and M. Gómez-Heras (2015), Influence of mineralogy on granite decay induced by temperature increase: Experimental observations and stress simulation, *Engineering Geology*, *189*, 58-67, doi:https://doi.org/10.1016/j.enggeo.2015.01.026.

Wang, M., and M. Cai (2020), A grain-based time-to-failure creep model for brittle rocks, *Computers and Geotechnics*, *119*, 103344, doi:https://doi.org/10.1016/j.compgeo.2019.103344.

Warren, J., and G. Hirth (2006), Grain size sensitive deformation mechanisms in naturally deformed peridotite, *Earth and Planetary Science Letters*, *248*, 438-450, doi:10.1016/j.epsl.2006.06.006.

Winter, J. K., F. P. Okamura, and S. Ghose (1979), A high-temperature structural study of high albite, monalbite, and the analbite--> monalbite phase transition, *American Mineralogist*, *64*(3-4), 409-423.

Wu, F., J. Chen, and Q. Zou (2019), A nonlinear creep damage model for salt rock, *International Journal of Damage Mechanics*, *28*(5), 758-771.

Wu, Z., X. Xu, Q. Liu, and Y. Yang (2018), A zero-thickness cohesive element-based numerical manifold method for rock mechanical behavior with micro-Voronoi grains, *Engineering Analysis with Boundary Elements*, *96*, 94-108, doi:https://doi.org/10.1016/j.enganabound.2018.08.005.

Yanagidani, T., S. Ehara, O. Nishizawa, K. Kusunose, and M. Terada (1985), Localization of dilatancy in Ohshima granite under constant uniaxial stress, *Journal of Geophysical Research: Solid Earth*, *90*(B8), 6840-6858, doi:https://doi.org/10.1029/JB090iB08p06840.

Yang, S.-Q., P. G. Ranjith, H.-W. Jing, W.-L. Tian, and Y. Ju (2017), An experimental investigation on thermal damage and failure mechanical behavior of granite after exposure to different high temperature treatments, *Geothermics*, *65*, 180-197, doi:https://doi.org/10.1016/j.geothermics.2016.09.008.

Zhou, H., C. Wang, B. Han, and Z. Duan (2011), A creep constitutive model for salt rock based on fractional derivatives, *International Journal of Rock Mechanics and Mining Sciences*, *48*(1), 116-121.